Energy & Environmental Science

ROYAL SOCIETY OF CHEMISTRY

PAPER

View Article Online
View Journal

Check for updates

Cite this: DOI: 10.1039/d6ee02327d

Suppressing dendrites *via* lateral lithium flux in Li metal solid-state batteries

Huanyu Zhang, †[ab] Faruk Okur, †[ab] Matthias Klimpel, [ab] Julian F. Baumgärtner, [ab] Jaka Šivavec, [ab] André Müller, [b] Ihor Neporozhnii, [c] Orhan Kibrisli, [c] Oleksandr Voznyy, [c] Yaroslav E. Romanyuk, [b] Maksym V. Kovalenko *[abd] and Kostiantyn V. Kravchyk *[ab]

Received 10th April 2026,
Accepted 26th May 2026

DOI: 10.1039/d6ee02327d

rsc.li/ees

Lithium dendrite growth at the lithium–solid-state electrolyte (SSE) interface, driven by void formation, remains a major barrier to the deployment of Li metal solid-state batteries. Here, we reveal a mechanism of lateral lithium flux that explains how interfacial layers (ILs) along the Li/SSE interface enable suppression of void formation, thereby preventing dendrite growth. Using Li_3Sb as a model IL and $Li_7La_3Zr_2O_{12}$ as a benchmark SSE, we directly visualize and quantify lateral lithium transport, demonstrating that ILs mitigate void formation by defocusing the local current density. This mechanism accounts for the cycling stability of IL-functionalized Li/SSE interfaces and provides design principles for safe, high-energy-density Li metal solid-state batteries.

Broader context

The transition to a low-carbon energy future depends critically on safer, high-energy-density batteries to support electric transportation and renewable electricity storage. Lithium metal solid-state batteries are widely regarded as a transformative technology because they promise substantially higher energy density while improving safety compared with conventional liquid-electrolyte systems. However, the large-scale deployment of solid-state batteries remains hindered by interfacial instability: microscopic voids form at the Li/solid-state electrolyte (SSE) interface due to uneven current distribution, ultimately triggering lithium dendrites that can cause short circuits. Addressing this challenge is essential for enabling durable batteries capable of meeting future global energy demands. This work uncovers a previously underexplored mechanism for stabilizing this interface: current defocusing driven by lateral lithium flux through mixed ionic-electronic interfacial layers. By directly visualizing and quantifying this lateral transport, and validating its effects through modeling and electrochemical testing, we establish design principles for stabilizing Li/SSE interfaces. These insights move the field beyond empirical interfacial engineering toward mechanism-guided strategies. More broadly, enabling reliable lithium metal solid-state batteries could accelerate electrification, support deeper renewable integration, and reduce the environmental footprint of energy storage technologies.

Introduction

Solid-state batteries stand at the forefront of next-generation energy storage, yet their practical deployment remains constrained by the instability of the Li/solid-state electrolyte (SSE) interface. During lithium stripping, microscopic voids form along this boundary, leading to contact loss and, upon subsequent Li plating, uncontrolled growth of lithium dendrites.[1,2]

At the heart of this problem lies current focusing, which refers to the uneven distribution of current density across the Li/SSE interface (Fig. 1A–D).[3–5] Such inhomogeneity can originate from a variety of microscopic surface imperfections, including impurities,[6–8] pre-existing voids,[9,10] grain boundaries,[11,12] or even subtle variations in surface roughness.[13,14] These local "hotspots" promote non-uniform lithium stripping and rapidly degrade interfacial stability.

Over the past few years, several strategies have been proposed to mitigate current focusing: applying stack pressure or elevated temperatures to maintain contact,[15] carefully cleaning or polishing SSE surfaces,[16–18] or introducing interfacial modifications.[19,20] Among these, the use of interfacial layers (ILs) at the Li/SSE boundary has proven particularly effective. ILs dramatically lower voltage polarization and enable extended

[a] Laboratory of Inorganic Chemistry, Department of Chemistry and Applied Biosciences, ETH Zürich, 8093 Zürich, Switzerland. E-mail: mvkovalenko@ethz.ch, kostiantyn.kravchyk@empa.ch
[b] Laboratory for Thin Films and Photovoltaics, Empa – Swiss Federal Laboratories for Materials Science & Technology, 8600 Dübendorf, Switzerland
[c] Department of Physical and Environmental Sciences, University of Toronto Scarborough, Scarborough, M1C 1A4, Canada
[d] Institute of Energy Science and Technology (SIEST), Sungkyunkwan University (SKKU), 2066, Seobu-ro, Jangan-gu, Suwon, Gyeonggi-do 16419, Republic of Korea
† HZ and FO contributed equally.

Open Access Article. Published on 27 May 2026. Downloaded on 6/17/2026 4:49:48 PM.
This article is licensed under a Creative Commons Attribution-NonCommercial 3.0 Unported Licence.

Open Access Article. Published on 27 May 2026. Downloaded on 6/17/2026 4:49:48 PM.
This article is licensed under a Creative Commons Attribution-NonCommercial 3.0 Unported Licence.

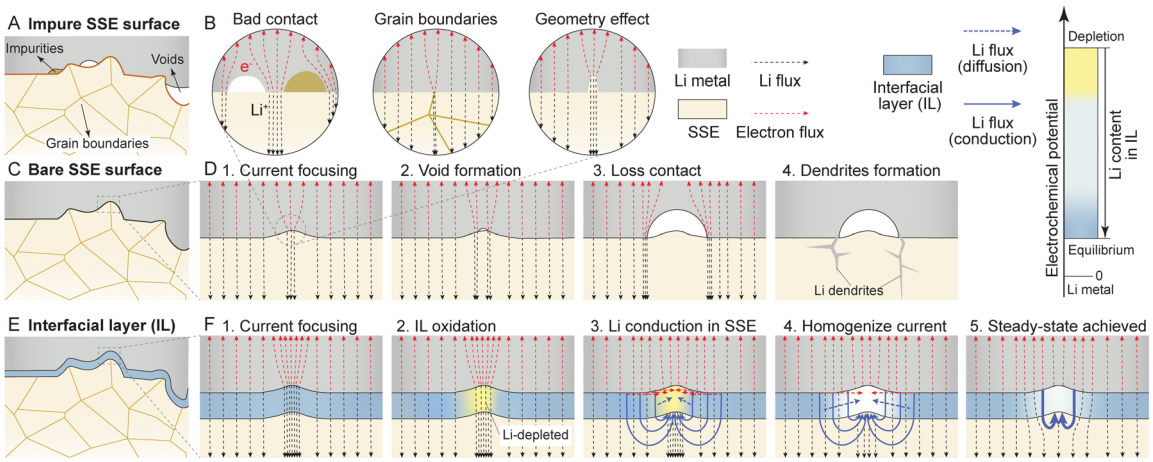

Fig. 1 Schematics of different Li/SSE interfaces based on (A) contaminated, (C) bare, and (E) IL-functionalized SSE surfaces. (B) Illustration of the origins of current focusing at the Li/SSE interface during lithium plating and stripping, arising from the poor interfacial contact, grain boundaries, and geometric irregularities. (D) Schematic of void and dendrite formation at the Li/SSE interface caused by current focusing. (F) Illustration of current homogenization at the Li/SSE interface enabled by lateral lithium flux through the IL.

Li cycling at high current densities (>1 mA cm^{-2}) and large areal capacities (>1 mAh cm^{-2}).[21] These improvements are generally attributed to enhanced lithiophilicity and reduced interfacial resistance.[22–24] However, such interpretations do not account for current focusing, which governs interfacial instability under practical conditions. As a result, the fundamental mechanism by which ILs regulate Li transport and enable stable cycling at the Li–SSE interface remains unclear.

Results and discussion

Current defocusing by lateral Li flux

The concept proposed here assumes that the IL can be any Li-containing compound that satisfies the following three conditions:[19,20] (1) its lithiation/delithiation potential lies close to the Li$^+$/Li redox potential, (2) it can undergo reversible lithiation/delithiation at an appropriate potential under operating conditions, and (3) in its lithiated state, it exhibits both Li-ion and electronic conductivity, *i.e.* it behaves as a mixed ionic-electronic conductor (MIEC). Under these requirements, many well-studied anode-active materials in the Li-ion battery field could serve as suitable IL candidates for current density defocusing. Examples include lithiated graphite,[25,26] Li–Mg,[9] Li–Sb,[27] Li–Ag,[22] and Li–Si[28,29] alloys, among others.

Fig. 1E and F illustrate the concept of current defocusing *via* lateral Li flux. Consider the case of Li stripping, where current focusing occurs locally at the Li/IL/SSE interface. Importantly, local Li depletion is not the origin of current focusing, but a dynamic consequence of it. Under current focusing conditions, the rate of Li extraction at local hotspots can exceed the rate of Li replenishment, leading to transient Li depletion in the interlayer. The elevated current density therefore drives local oxidation of the IL, resulting in the formation of a Li-depleted (partially delithiated) region with higher chemical and electrochemical potential than the surrounding lithiated IL.

In response to this potential gradient, two transport processes arise. First, according to Fick's law, the difference in lithiation chemical potentials between the delithiated IL region, the lithiated IL, and the Li metal drives diffusion of Li atoms, indicated by blue dashed lines in Fig. 1F. Importantly, this flux is not confined to the vertical direction; it also proceeds laterally, causing Li atoms to migrate from the Li metal, through the lithiated IL, toward the delithiated IL region.

Second, the redox potential difference between metallic Li and the delithiated IL region, separated by either the lithiated IL or lithiated IL–SSE, provides the basis for an electrochemical mechanism of Li-ion transport, shown by blue solid lines in Fig. 1F. Although the IL is thermodynamically stable in its fully lithiated state under equilibrium conditions (Fig. 1B), local current focusing can give rise to significant amplification of current density and electrochemical potential at hot-spots, driving non-equilibrium delithiation.[30,31] Such localized amplification is an inherent consequence of current focusing and is not specific to any particular interlayer system. Under these conditions, even thermodynamically stable interlayers can undergo local oxidation or delithiation, provided that their redox potential lies sufficiently close to that of Li.

Specifically, Li can be oxidized at the Li/IL interface, generating Li$^+$ ions and electrons. The electrons migrate through the Li metal or lithiated IL, while the Li$^+$ ions move through the lithiated IL and/or through the bulk of the SSE. This flux proceeds laterally, nearly perpendicular to the applied electric field, thereby delivering Li into the delithiated IL region and mitigating void formation at the hot-spot. In essence, this process enables Li to be drawn from a much broader area than the hot-spot of the SSE surface. Importantly, this redistribution does not imply that Li-ion flux within the SSE becomes homogeneous, which remains concentrated near the hot spot where current focusing originates, as shown in Fig. 1F.

This journal is © The Royal Society of Chemistry 2026

Open Access Article. Published on 27 May 2026. Downloaded on 6/17/2026 4:49:48 PM.
This article is licensed under a Creative Commons Attribution-NonCommercial 3.0 Unported Licence.

Visualization of lateral Li flux at the IL/SSE interface

To validate the proposed concept of current defocusing, we designed an experiment that allows direct monitoring of the lateral reaction kinetics between lithium and an Sb film, which is a commonly employed interfacial layer at the Li/SSE interface (Fig. 2). Sb was selected for several reasons. Beyond fully satisfying the criteria outlined above, namely, its MIEC character in the lithiated state[32,33] and its redox potential near that of the Li metal,[34] the lithiation of Sb yields Li_2Sb and Li_3Sb alloys that are readily distinguishable from pristine Sb by color. This clear visual contrast enables direct monitoring of the surface reaction rate between the Sb film and metallic Li. For the substrate, we employed the Li-ion-conducting garnet-type LLZO SSE, chosen for its electrochemical stability against metallic Li.[35,36] The chemical stability of LLZO ensured that any observed reaction could be attributed to Sb lithiation, thereby excluding possible artifacts arising from parasitic reactions between the SSE and Li. The details of fabrication of the LLZO SSE as well as its characterization are provided in the supplementary information (SI) and the Methods section.

The experiments were carried out as follows. A 10 nm layer of Sb was magnetron-sputtered on the Li-ion conducting substrate (LLZO membrane). Li foil was then applied to the Sb-coated region *via* cold-isostatic pressing (CIP), followed by heating to different temperatures of 25 °C (RT) up to 275 °C, while monitoring the formation of two additional regions with distinct colors on the Sb-coated LLZO surface over time (Fig. 2A, Fig. S4–S8 and Videos S1–S3). Importantly, the alloys progressively extended into regions without direct Li coverage, clearly illustrating the lateral propagation of the reaction front. Grazing-incidence X-ray diffraction (GIXRD) confirmed that these color changes correspond to the formation of Li_3Sb and Li_2Sb alloys (Fig. S9). As demonstrated in Fig. 2B, once Li_3Sb and Li_2Sb formed near the Li metal, a sequence of processes unfolded over time: lithium transports from metallic Li toward the Li_2Sb/Li_3Sb interface, forming new Li_3Sb (Reaction (1), Rx_1), while simultaneously migrating toward the Li_2Sb/Sb interface to generate additional Li_2Sb (Reaction (2), Rx_2).

Notably, analogous experiments performed on non-Li-ion-conducting substrates showed strongly suppressed lateral propagation of the Li_3Sb or Li_2Sb regions over time (Fig. 2C and Fig. S10). This observation demonstrates that the lateral Li flux is not driven by the chemical potential difference between the Li metal and Sb, which would promote diffusion of Li atoms toward Sb, but rather by the redox potential difference between Li and Sb, which drives Li^+ ions through the Li-ion-conducting LLZO electrolyte. The latter process is analogous to a battery-like redox mechanism, as illustrated in Fig. S11, and can be described as follows. The Li metal at the Li/SSE interface can be oxidized to form Li^+ ions and electrons as a consequence of the electrochemical potential gradient with the adjacent Sb layer. The electrons migrate through the Li_3Sb layer toward Sb, while

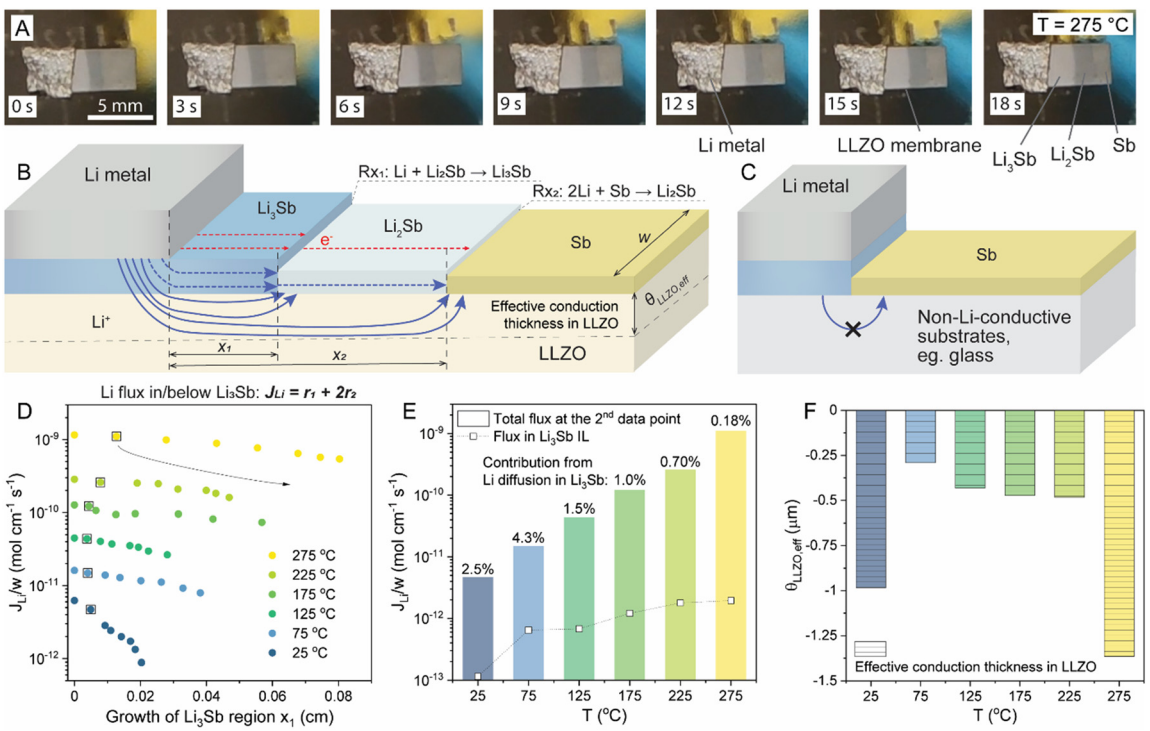

Fig. 2 Visualization of lateral lithium flux at the Li/Li_3Sb IL/SSE interface. (A) Photographs showing the formation of Li_2Sb and Li_3Sb alloys at 275 °C on an Sb-sputtered LLZO substrate. Schematics illustrating surface reactions occurring on (B) a Li-ion-conductive LLZO substrate and (C) a non-Li-ion-conductive substrate. (D) Experimentally measured Li flux during the formation of Li_2Sb and Li_3Sb across the Li_3Sb region at various temperatures as a function of its length. (E) Contribution of Li diffusion within Li_3Sb to the total measured lateral Li flux. (F) Calculated effective thickness of Li-ion transport in LLZO as a function of temperature.

Open Access Article. Published on 27 May 2026. Downloaded on 6/17/2026 4:49:48 PM.
This article is licensed under a Creative Commons Attribution-NonCommercial 3.0 Unported Licence.

the Li^+ ions are transported through the Li_3Sb and along the SSE. At the Sb/LLZO interface, the two charge carriers recombine, driving the lithiation of Sb to form Li_3Sb. This mechanism is effectively equivalent to the self-discharge process of a Sb/LLZO/Li cell, as illustrated in Fig. S11c, d and Video S4. In these experiments, the progressive formation of differently colored regions, corresponding to Li_2Sb and Li_3Sb alloys, was clearly observed during discharge.

Quantification of lateral Li flux at the IL/SSE interface

Next, by tracking the expansion rates of the Li_3Sb and Li_2Sb regions (x_1 and x_2), we quantified the total lateral Li flux through the LLZO SSE by summing the Li consumption rates of the Rx_1 and Rx_2 reactions (Fig. 2B). The resulting flux values were plotted as a function of temperature (Fig. 2D; see Fig. S12, S13 and Methods for details). The observed non-linear propagation behavior arises from distance-dependent transport resistance, as both Li-ion conduction through the SSE and Li diffusion within the interlayer decrease with increasing transport distance, as demonstrated in eqn (7) and (11). Importantly, temperature is varied to accelerate the lateral propagation of the reaction front, enabling direct visualization of transport behavior within experimentally accessible timescales. The consistent observation of lateral Li transport across this temperature range further supports the robustness of the proposed mechanism.

Since these fluxes include contributions from both Li-atom diffusion and Li-ion transport within LLZO, we subsequently isolated the Li-ion conduction component by subtracting the Li diffusion contribution. The diffusion-driven flux was estimated using Fick's law, consistent with the Li diffusion coefficient in Li_3Sb obtained from molecular dynamics (MD) simulations (see Fig. S14 for details). Notably, these analyses revealed that Li diffusion accounts for less than 5% of the total lateral flux (Fig. 2E), underscoring the dominant role of Li-ion transport driven by the redox potential difference between the Li metal and Sb ($E^0_{Sb/Li_2Sb} = 0.90$ V *vs.* Li^+/Li) or Li_2Sb ($E^0_{Li_2Sb/Li_3Sb} = 0.85$ V *vs.* Li^+/Li).[34] Using this potential difference, the Li-ion conductivity of LLZO, and the lateral distance of the Li_3Sb region, we also estimated, *via* Ohm's law, the effective thickness of Li-ion transport in LLZO. The calculated values fall in the range of 0.25–1.5 μm depending on the temperatures (Fig. 2F). Notably, the lateral Li-ion current density at 75 °C was determined to be substantial at ~47 mA cm^{-2} (Fig. 2E).

To further estimate the magnitude of lateral current density in a configuration more closely resembling a practical symmetrical cell, we modeled Li flux in a Li/Li_3Sb(Sb)/LLZO/Li system at an applied current density of 50 mA cm^{-2}. Specifically, we examined the Li flux distribution following a current-focusing event in an LLZO SSE coated with a 20 nm Li_3Sb interlayer, where the central 10 nm region of the IL was assumed to be fully oxidized to Sb. Finite element modeling (FEM) of the Li flux distribution (Fig. 3A) and the potential distribution generated by the hot-spot (Fig. 3B) within the LLZO SSE was performed using the FEniCS computing platform (see Methods for

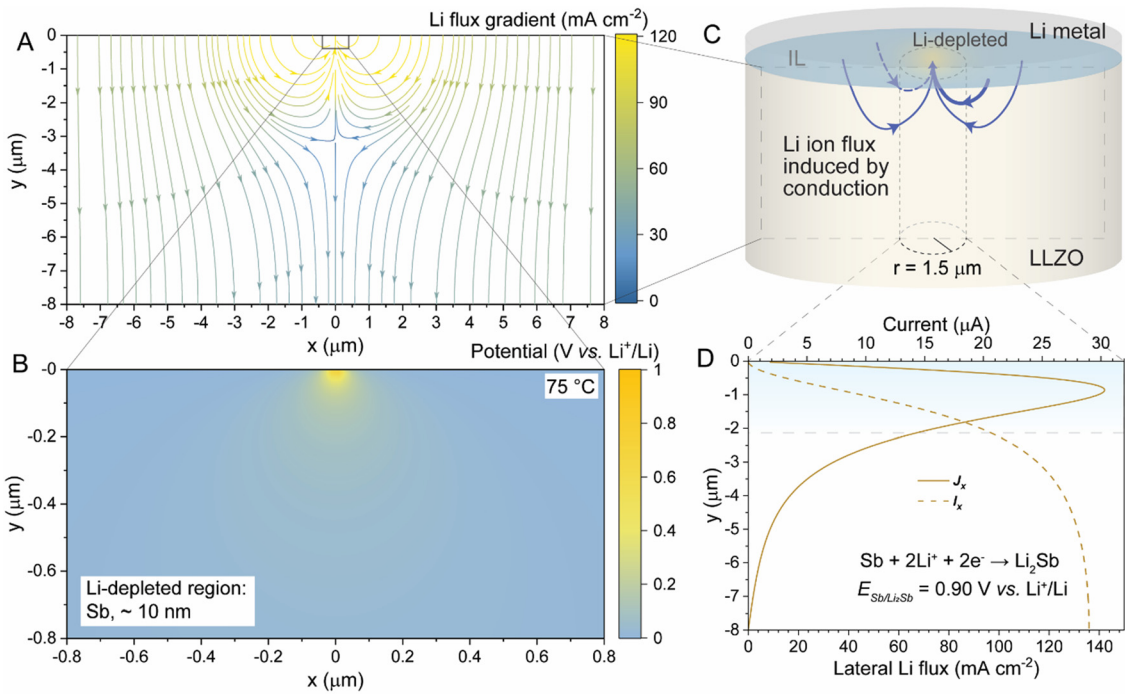

Fig. 3 Evaluation of lateral Li flux. (A) Two-dimensional Li-ion flux distribution map and (B) corresponding potential map across a Li/Li_3Sb(Sb)/LLZO/Li cell at an applied current density of 50 mA cm^{-2}, obtained from finite element modeling. (C) Schematic of the modeled Li/Li_3Sb(Sb)/LLZO/Li cell, where the central 10 nm region of the Li_3Sb IL was assumed to be fully oxidized to Sb. (D) Lateral Li-ion current density profile and total lateral current integrated over the surface of a cylindrical region with a 1.5 μm radius within the LLZO SSE.

This journal is © The Royal Society of Chemistry 2026

Open Access Article. Published on 27 May 2026. Downloaded on 6/17/2026 4:49:48 PM.
This article is licensed under a Creative Commons Attribution-NonCommercial 3.0 Unported Licence.

details). The results show the spatial distribution of Li-ion current within the SSE. In particular, the modeling highlights the lateral component of the flux, which arises from the redox potential difference between the Li-covered LLZO surface and the locally Li-depleted (Sb) region. This redox-driven mechanism generates a substantial lateral Li-ion current inside the LLZO SSE, thereby redistributing the flux away from the hot-spot.

Interestingly, analysis of the Li flux and the corresponding current density on the lateral surface surrounding the Li-depleted region revealed that the flux peaks at a depth of *ca.* 1 μm and decreases toward 4 μm beneath the Li_3Sb/LLZO interface (Fig. 3D). By integrating the current density over the surface of the column with a radius of 1.5 μm (Fig. 3C), the total induced lateral current was estimated to be ~29 μA. This allowed us to calculate the lithiation rate of the Li-depleted Sb region, which can occur in as little as ~10 ns once the applied current density of 50 mA cm^{-2} is removed. This finding indicates that current density homogenization *via* lateral Li flux can be achieved on the nanosecond timescale. Notably, simulations assuming partial oxidation of the IL to Li_2Sb (Fig. S15) showed similar results.

Effectiveness of the Li_3Sb IL

Next, to demonstrate the effectiveness of the Li_3Sb IL in homogenizing the LLZO/Li interface and mitigating void formation, we prepared and electrochemically characterized two Li/LLZO/Li symmetrical cells, with and without the Li_3Sb IL, using LLZO membranes prepared under identical conditions. Considering the critical impact of the SSE thickness on both energy density and voltage polarization, we selected 45 μm-thick LLZO membranes (rather than millimeter-thick pellets) to ensure that the LLZO/IL/Li system could be directly applied in high-energy-density full-cell architectures.[37] The interfacial resistance of the Li_3Sb/LLZO interface and the total resistance of the symmetrical cell were measured to be as low as *ca.* 0.13 Ω cm^2 and 1.3 Ω cm^2, respectively, at 75 °C (Fig. S16).

Although the degree of current density homogenization with the Li_3Sb IL cannot be measured directly, voltage profiles from critical current density (CCD) measurements can provide qualitative indication of current density defocusing. Specifically, markedly flatter voltage profiles of symmetrical cells with the IL should indicate substantial mitigation of void formation at equivalent current densities compared with the cell without the IL. Indeed, as shown in Fig. 4, the cell without the IL maintained a quasi-stable stripping regime (flat voltage profiles) only up to a current density of 12 mA cm^{-2}, exhibiting a CCD of 16 mA cm^{-2}. In contrast, the system with the Li_3Sb IL preserved the quasi-stable stripping regime up to *ca.* 40 mA cm^{-2} and thus exhibited a markedly higher CCD of 70 mA cm^{-2}, demonstrating the effectiveness of the Li_3Sb IL in homogenizing the current and suppressing void formation.

Notably, direct experimental observation of such Li-depleted regions remains challenging due to their nanoscale spatial extent and transient nature under non-equilibrium conditions. The mechanistic interpretation presented here is therefore supported by indirect evidence, including the observed lateral propagation of alloy phases, quantitative flux analysis, and consistency with electrochemical behavior and modeling.

Role of lateral Li flux during plating

While the proposed mechanism is primarily activated during Li stripping, its impact extends to subsequent Li plating processes. In solid-state systems, void formation during stripping often precedes dendrite growth during plating, as loss of interfacial contact leads to severe current focusing upon reversal of current. By mitigating local Li depletion and maintaining interfacial contact, lateral Li transport reduces current inhomogeneity during subsequent plating, thereby suppressing dendrite nucleation.

Under plating conditions, the interlayer is already in a Li-rich state and does not undergo further significant lithiation. Therefore, a depletion-driven mechanism analogous to stripping is not expected. Instead, the interlayer contributes by enabling

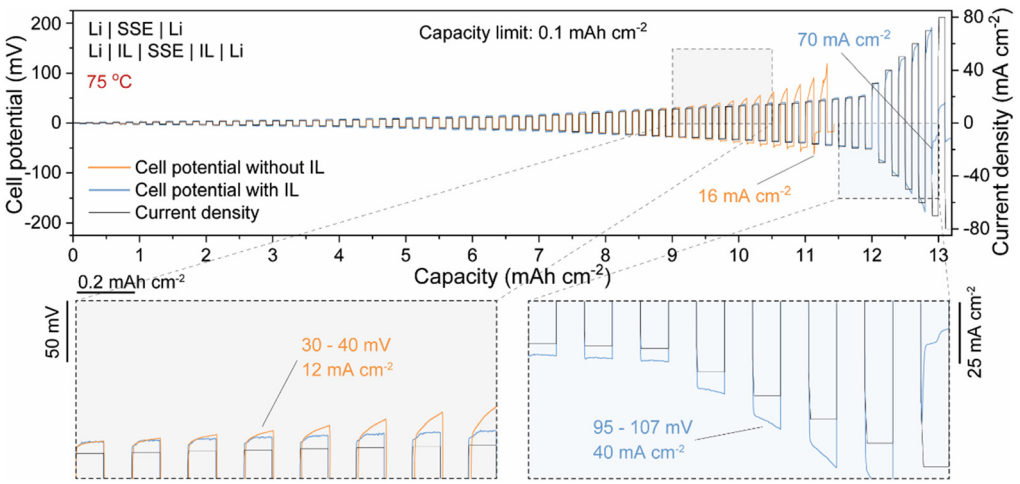

Fig. 4 CCD measurements of Li/LLZO/Li symmetric cells with and without the Li_3Sb IL. Voltage profiles of Li/LLZO/Li symmetric cells measured at various current densities with a capacity limit of 0.1 mAh cm^{-2} per half-cycle.

Open Access Article. Published on 27 May 2026. Downloaded on 6/17/2026 4:49:48 PM.
This article is licensed under a Creative Commons Attribution-NonCommercial 3.0 Unported Licence.

more uniform distribution of ionic and electronic flux, further stabilizing Li deposition.

Prolonged cycling of the Li metal anode with the Li_3Sb IL

To evaluate the effectiveness of the Li_3Sb alloy as an IL between the Li metal and LLZO during prolonged plating and stripping, we performed galvanostatic cycling of Li/LLZO/Li symmetric cells with and without the Li_3Sb IL. The tests were conducted without applied pressure, starting at low current densities (0.1–2 mA cm^{-2}) and then increasing stepwise to 3 mA cm^{-2} for cells without the IL and 4 mA cm^{-2} for cells with the IL. In both cases, the areal capacity was limited to 1 mAh cm^{-2}.

Importantly, as shown in Fig. 5A, the Li/LLZO/Li cell without the Li_3Sb IL exhibited significant voltage polarization after only a few cycles at a current density of 3 mA cm^{-2} and eventually short-circuited, due to the formation of voids at the Li/LLZO interface (Fig. 5B and C), consistent with the CCD measurements. In contrast, the cell with the Li_3Sb IL maintained a stable overpotential for over 900 hours and delivered a cumulative capacity of over 3400 mAh cm^{-2} at a high current density of 4 mA cm^{-2}, without any voltage polarization (Fig. 5D and Fig. S17). This performance is in line with cross-sectional FIB-SEM measurements, demonstrating conformal contact between the lithium metal and Sb-covered LLZO (Fig. 5E and F) even after long-term cycling. Furthermore, EIS measurements performed every 10 cycles on the complementary Li/Li_3Sb/LLZO/Li_3Sb/Li cell (Fig. 5G and Fig. S18) showed that the total resistance remained below 4 Ω cm^2 over 3000 cycles, even at a high current density of 4 mA cm^{-2}. Notably, the stable values of interfacial resistance indicate significant mitigation of void formation in the presence of the Li_3Sb IL during prolonged cycling.

In the context of the stability of the Li_3Sb IL during Li plating/stripping, two additional aspects are noteworthy to discuss. First, the formation energy of Li_3Sb is significantly lower than that of other Li–M alloys (Fig. S19), indicating its chemical stability and minimizing Sb diffusion into bulk Li. This contrasts with alloys such as Li–Ag or Li–Mg, which have been reported to undergo Ag or Mg migration into Li.[38,39] Second, although the high electronic conductivity of ILs could, in principle, allow Li to plate at the IL/SSE interface and displace the IL, the stable overpotentials observed in Li_3Sb IL cells suggest this does not occur. To further examine the stability of the Li_3Sb interlayer during Li plating, ~2 μm of Li was plated onto the Li_3Sb/LLZO interface in a symmetric cell, followed by energy-dispersive X-ray spectroscopy (EDS) measurements. EDS was used to probe the spatial distribution of Sb across the Li/IL/LLZO interfaces. The results (Fig. S20) show that Sb remains localized at the LLZO surface after Li deposition, indicating that the Li_3Sb interlayer is preserved at the interface during plating. This observation is consistent with the absence of interlayer displacement during Li plating.

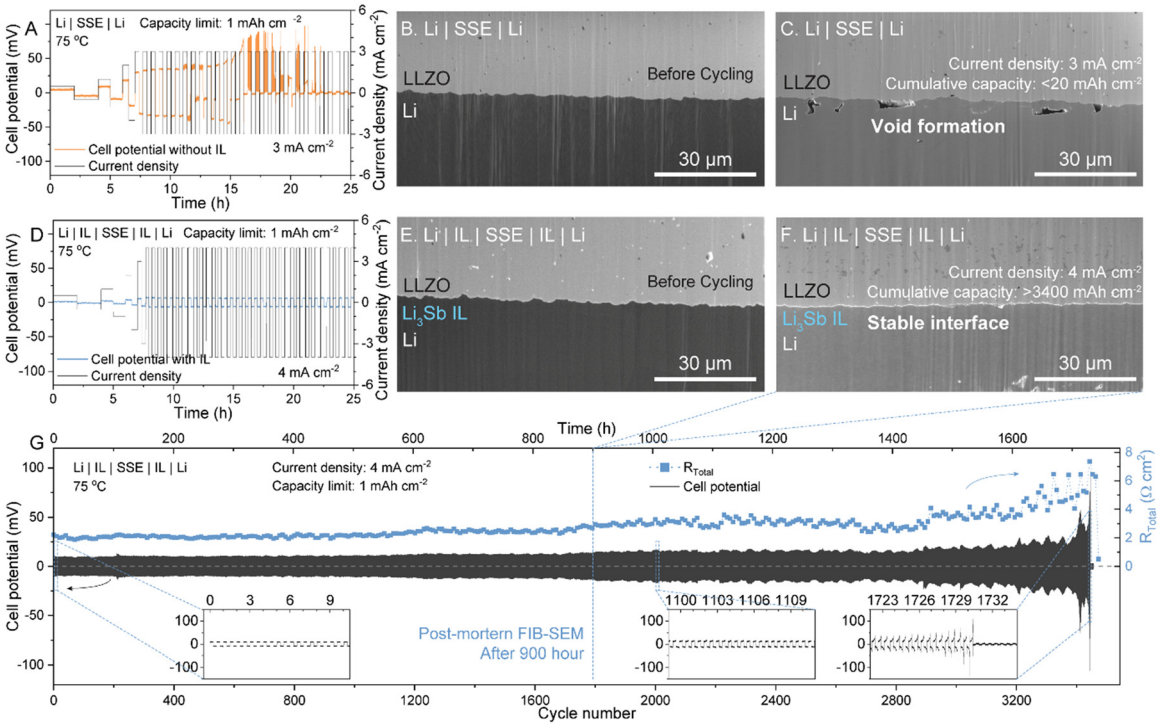

Fig. 5 Cyclic stability of Li/LLZO/Li symmetric cells with and without the Li_3Sb IL. (A) Voltage profiles of a Li/LLZO/Li symmetric cell and corresponding FIB-SEM cross-sections (B) before and (C) after short-circuiting. (D) Voltage profiles of a Li/Li_3Sb/LLZO/Li_3Sb/Li symmetric cell and FIB-SEM cross-sections (E) before and (F) after cycling to a cumulative capacity of 3400 mAh cm^{-2}. The extended voltage profile is shown in Fig. S17. (G) Voltage profile of the Li/Li_3Sb/LLZO/Li_3Sb/Li symmetric cell cycled at 4 mA cm^{-2} with a capacity limit of 1 mAh cm^{-2} per half-cycle, with total cell resistance determined by EIS measurements performed every 10 cycles. Corresponding impedance spectra are provided in Fig. S18.

This journal is © The Royal Society of Chemistry 2026

Open Access Article. Published on 27 May 2026. Downloaded on 6/17/2026 4:49:48 PM. This article is licensed under a Creative Commons Attribution-NonCommercial 3.0 Unported Licence.

Following the electrochemical assessment of the Li metal anode with the Li_3Sb-coated LLZO SSE using symmetric cells, we extended our investigation to an all-solid-state full cell configuration, utilizing $LiNi_{0.8}Mn_{0.1}Co_{0.1}O_2$ (NMC811) as the cathode active material and Li_6PS_5Cl (LPSCl) as the catholyte (Fig. S21 and in Note S3). The gravimetric and volumetric energy densities of the NMC811-LPSCl/LLZO/Li_3Sb/Li full cell were estimated to be *ca.* 163 Wh kg^{-1} and 611 Wh L^{-1}, respectively. Importantly, as indicated by the energy density calculations, both values can be significantly increased to 250 Wh kg^{-1} and 700 Wh L^{-1} by employing a higher loading of the NMC811 cathode active material (25 mg cm^{-2}; Fig. S22 and Table S2).

Conclusions

This work reveals the mechanism of current defocusing at the Li/SSE interface, driven by lateral lithium flux through ILs that enable long-term cycling of Li metal anodes. Using Li_3Sb as a model mixed ionic-electronic conducting IL and LLZO as a benchmark SSE, we directly visualized and quantified lateral Li transport, showing that it redistributes current density, suppresses void formation, and prevents dendrite initiation. Finite element modeling confirmed that redox-driven Li-ion transport within the SSE generates strong lateral currents on nanosecond timescales, rapidly homogenizing the Li/IL/SSE interface. Symmetric Li/LLZO/Li cells with Li_3Sb ILs reached critical current densities above 70 mA cm^{-2} and cycled stably for over 900 h without pressure at a high current density of 4 mA cm^{-2} with an areal capacity limit of 1 mAh cm^{-2}. More broadly, the concept of current defocusing by lateral Li flux provides a framework for further design of the Li/SSE interface by leveraging redox-driven lateral Li transport and eventually opens a new route toward intrinsically safe, Li metal solid-state batteries.

Methods

Fabrication of LLZO membranes

LLZO membranes were fabricated following procedures detailed in ref. 37. The process involved several key steps: preparation of the LLZO slurry, tape casting, drying, delamination from the substrate, debinding, and ultra-fast sintering, as described below. The slurry was prepared by ball milling 3 g of LLZO powder ($Li_{6.25}Al_{0.25}La_3Zr_2O_{12}$, 99.9%, D_{50} = 400–600 nm, Ampcera) with a solution consisting of 8 vol% plasticizer (G-260, Sekisui Chemical), 7.6 vol% surfactant (Malialim, NOF Corporation), and 84 vol% solvent mixture isopropanol (Emsure) : ethanol (Sigma-Aldrich) : 1-propanol (99.5%, Acro-Seal) = 5 : 87 : 8) at 165 rpm for 18 hours. Subsequently, a binder solution polyvinyl butyral (PVB – BL-7Z, Sekisui Chemical, Mw 3.91×10^4) : isopropanol = 30 : 60 wt%) was added (2 mL) and further mixed at 200 rpm for 2 hours. The LLZO slurry was tape-cast onto a glass substrate using a doctor-blade with a 400 μm opening at a speed of 1 mm s^{-1}. After drying in air at room temperature for 30 minutes, the tape-casted layer was peeled off and laser cut into 10 mm diameter discs. The discs were then debinded under O_2 flow in a muffle furnace according to the following schedule: 150 °C for 2 hours, 300 °C for 2 hours, and 600 °C for 2 hours (ramp rate of 300 °C h^{-1}). Ultra-fast sintering was performed in an Ar-filled glovebox. Debinded membranes were placed in a graphite envelope sandwiched between boron nitride plates and sintered at 1200 °C for 50 seconds using a custom-made setup. To remove surface Li_2O contamination, the sintered LLZO membranes were subjected to additional heat treatment at 900 °C for 10 minutes in an Ar-filled glovebox.

Sputtering of Sb

Sb was deposited onto LLZO membranes at room temperature using radio frequency magnetron sputtering (Orion, AJA International Inc.). The films were sputtered under an Ar flow of 50 sccm using an Sb target (99.999–99.99999%, Plasmaterials). The film thickness was controlled by measuring the deposition rate with a quartz crystal microbalance (QCM) and adjusting the deposition time accordingly. The fabrication process is demonstrated in Fig. S1.

Measurements of lateral Li flux during the Li–Sb alloy formation process

First, a rectangular LLZO membrane was coated with a 10 nm Sb film *via* magnetron sputtering. A part of this coated surface was then isostatically pressed with Li foil at 71 MPa. The Li foil was prepared by cutting a Li metal rod (99.9%, Sigma-Aldrich) into small pieces, rolling them on a stainless-steel substrate to a thickness of *ca.* 100 μm, and then cutting it into a rectangular shape. Next, the LLZO membranes with the attached Li foil were placed inside 20 mm-diameter coin cell casings and subjected to heat treatment at various temperatures (75, 125, 175, 225, and 275 °C) in an Ar-filled glovebox. The evolution of the Sb-coated LLZO surface was monitored in real time using a camera (Fig. 2A, Fig. S4–S8 and Videos S1–S3). Monitoring at room temperature began after isostatic pressing of the Li foil on the Sb-coated LLZO surface. The recorded images were subsequently processed using ImageJ software (Fig. S12). The time origin (0 s) is defined as the moment when the sample is placed on the pre-heated stage. Due to rapid thermal equilibration, some initial reaction may already have occurred before optical recording begins.

Considering that GISXRD measurements confirmed that the reaction between the Li foil and the Sb-coated LLZO surface resulted in the formation of two distinct regions in close proximity to the Li metal, corresponding to Li_2Sb and Li_3Sb alloys, processes occurring over time during Li isostatic pressing on the Sb-coated LLZO surface followed by heat treatment can be summarized as follows. The isostatic pressing of Li causes its immediate chemical reaction with Sb, resulting in the formation of the Li_3Sb alloy located below the Li foil and in close proximity to the edge of the Li foil, as well as the formation of the small Li_2Sb alloy region between Li_3Sb and Sb, as illustrated in Fig. 2A and Fig. S9. Then a few processes unfold over time, and Li is transported from the Li metal through the Li_3Sb region towards the Li_2Sb/Li_3Sb boundary,

Open Access Article. Published on 27 May 2026. Downloaded on 6/17/2026 4:49:48 PM.
This article is licensed under a Creative Commons Attribution-NonCommercial 3.0 Unported Licence.

where it reacts with Li_2Sb to generate a new Li_3Sb region (Reaction (1), Rx_1). Subsequently, Li continues to pass through the Li_2Sb region, reacting with pure Sb to form the new Li_2Sb phase (Reaction (2), Rx_2).

The calculations of lateral Li flux were done based on the assumption that the alloying process only leads to the expansion of the thickness (θ, nm), while the width of the alloy regions (w, cm, the width of the LLZO membranes) remains constant and the length of the regions (x, cm) does not change due to the alloying process. Therefore, the thicknesses of the formed Li_3Sb and Li_2Sb alloys were calculated based on the thickness of the magnetron-sputtered Sb film (θ_{Sb} = 10 nm) considering $n_{Li_3Sb} = n_{Li_2Sb} = n_{Sb}$ mass balance and the molar concentration of each solid phase per unit volume (c, mol cm^{-3}):

$$c_{Li_3Sb}\theta_{Li_3Sb} = c_{Li_2Sb}\theta_{Li_2Sb} = c_{Sb}\theta_{Sb} \quad (1)$$

Notably, molar concentrations of Sb, Li_2Sb and Li_3Sb phases per unit volume were assumed to be constant in the temperature range of 25–275 °C, which were calculated by dividing their density (ρ, g cm^{-3}) by molar mass (M, g mol^{-1}), assuming that they remained constant at temperatures from 25 to 275 °C:

$$c = \frac{\rho}{M} \quad (2)$$

The reaction rate of Reactions (1) and (2) (consumptions of Li_2Sb for Reaction (1) and consumption of Sb for Reaction (2), r_1 and r_2, mol s^{-1}) were calculated by normalization of the width (w) using the following equations and Fig. S4:

$$r_1 = \frac{dn_{Li_2Sb}}{dt} = c_{Li_2Sb}\frac{dV_{Li_2Sb}}{dt} = c_{Li_2Sb}\theta_{Li_2Sb}w\frac{dx_1}{dt}$$

$$r_1/w = c_{Li_2Sb}\theta_{Li_2Sb}\frac{dx_1}{dt} \quad (3)$$

$$r_2 = \frac{dn_{Sb}}{dt} = c_{Sb}\frac{dV_{Sb}}{dt} = c_{Sb}\theta_{Sb}w\frac{dx_2}{dt}$$

$$r_2/w = c_{Sb}\theta_{Sb}\frac{dx_2}{dt} \quad (4)$$

where x_1 is the length of the consumed Li_2Sb region and x_2 is the length of the consumed Sb region, as illustrated in Fig. 2B and Fig. S11.

The lateral Li flux in the Li_3Sb region (J_{Li}/w, mol cm^{-1} s^{-1}), which is the sum of consumption rates of Li_2Sb and Sb ($J_{Li} = r_1 + 2r_2$, mol s^{-1}), can be calculated as follows:

$$J_{Li} = c_{Li_2Sb}\theta_{Li_2Sb}w\frac{dx_1}{dt} + 2c_{Sb}\theta_{Sb}w\frac{dx_2}{dt}$$

$$J_{Li}/w = c_{Li_2Sb}\theta_{Li_2Sb}\frac{dx_1}{dt} + 2c_{Sb}\theta_{Sb}\frac{dx_2}{dt} \quad (5)$$

Considering measured values of x_1 and x_2 at different temperatures as a function of time, we have calculated values of r_1, r_2, and J_{Li}, which were then plotted as a function of time at different temperatures (Fig. S13).

The position of the reaction front was determined from optical images with a spatial resolution of 0.03236 mm per pixel. An uncertainty of ±3 pixels (±0.1 mm) was assumed for the determination of the reaction front position. The temporal resolution of the measurement was 0.1 s. The uncertainty in the propagation rate (dx/dt) was estimated using standard error propagation, with the spatial resolution as the dominant contribution. The resulting relative uncertainty is on the order of a few percent, while the contribution from temporal resolution is negligible. Error bars in Fig. S12 and S13 reflect these uncertainties.

Calculation of Li diffusion in Li_3Sb by molecular dynamics

We conducted molecular dynamics (MD) simulations of the Li_3Sb system to investigate its ionic conductivity in the presence of lithium vacancies. Two models were studied: one with a single Li vacancy and another with four vacancies per supercell. Our results show that systems with a greater number of vacancies demonstrate higher ionic conductivity at elevated temperatures (Fig. S14). The calculated activation energies for Li_3Sb with one and four vacancies are 99.6 meV and 153.7 meV, respectively.

All the molecular dynamics (MD) simulations were performed using the Vienna *ab initio* simulation package (VASP)[40] based on periodic plane-wave density functional theory (DFT). The exchange and correlation interactions between electrons were treated within the generalized gradient approximation (GGA)[41] with the Perdew–Burke–Ernzerhof (PBE)[42] parameterization. The interactions between ion cores and valence electrons were described by the projector-augmented wave (PAW)[43] pseudopotentials with the energy cutoff set to 400 eV. The convergence threshold for the electronic self-consistent field (SCF) cycle was set to 10^{-5} eV. The k-point sampling was restricted to the Gamma point. The simulations were carried out in the canonical (NVT) ensemble, maintaining target temperatures of 300 K, 548 K, and 900 K. For all MD simulations the machine learning force fields (MLFF) were used, and the time step was set to 2 fs. As a model system a $Fm\bar{3}m$ cubic Li_3Sb 2 × 2 × 2 supercell was used with a 13.089 Å unit cell side. To simulate vacancies, one or four Li atoms were removed from the system before the MD simulation for Li_3Sb with one vacancy and four vacancies, respectively. All systems were first equilibrated for 10 ps, followed by a run of 1990 ps, from which trajectory data were collected for analysis. The analysis of MD trajectories was performed using the Pymatgen Analysis Diffusion package.[44,45]

Calculation of Li flux in Li_3Sb by Fick's law

Next, considering that the Li flux across the Li_3Sb region is driven by the concentration gradient of Li between the Li metal and Li_2Sb, we calculated Li flux J_{D,Li_3Sb} (mol cm^{-2} s^{-1}) in Li_3Sb at various temperatures, following Fick's law:

$$J_{D,Li_3Sb} = -D\frac{dc}{dx} = -D\frac{c_{Li\text{ in }Li_2Sb} - c_{Li\text{ in Li metal}}}{x_{Li_2Sb} - x_{Li}} = D\frac{\Delta c}{\Delta x} \quad (6)$$

where Δc (mol cm^{-3}) is the constant concentration difference between Li in Li metal and Li in Li_2Sb assuming that the concentration does not change with temperature, D (cm^2 s^{-1}) is the diffusion coefficient calculated by MD simulations with

 This journal is © The Royal Society of Chemistry 2026

Open Access Article. Published on 27 May 2026. Downloaded on 6/17/2026 4:49:48 PM. This article is licensed under a Creative Commons Attribution-NonCommercial 3.0 Unported Licence.

data in Table S1, and Δx (cm) is the distance between Li and Li_2Sb regions (x_1). The Li flux in Li_3Sb normalized by width J_D/w (mol cm^{-1} s^{-1}) can be calculated with the thickness of Li_3Sb θ_{Li_3Sb}:

$$J_D/w = J_{D,Li_3Sb}\theta_{Li_3Sb} = \theta_{Li_3Sb}D\frac{\Delta c}{\Delta x} \quad (7)$$

Calculation of the effective conduction thickness in LLZO

The calculation of the effective conduction thickness in LLZO $\theta_{LLZO,eff}$ (μm), shown in Fig. 2F, is simplified to the calculation of the width of two batteries: Li_2Sb/LLZO//Li_3Sb/Li and Sb/LLZO/Li_3Sb/Li, Fig. S11b. The resistance of LLZO in these two batteries can be calculated using the ionic conductivity of LLZO σ_{LLZO} from the Arrhenius equation in Fig. S2c and Table S1:

$$R_1 = \frac{x_1}{\sigma_{LLZO} w \theta_{LLZO,eff}} \quad (8)$$

$$R_2 = \frac{x_2}{\sigma_{LLZO} w \theta_{LLZO,eff}} \quad (9)$$

The voltage of these two batteries can be estimated using the electrochemical potential difference of Li_2Sb/Li_3Sb (U_1 = 0.85 V *vs.* Li^+/Li) and Sb/Li_2Sb (U_2 = 0.90 V *vs.* Li^+/Li), respectively. The electrochemical potential of the Li–Sb alloy is taken from ref. 41. The total current I (A) can be calculated using the lateral Li flux, as shown in Fig. 2E,

$$I = zFJ_{Li\ in\ LLZO} \quad (10)$$

where z is 1 and F is the Faraday constant, 96 385 s A mol^{-1}. The current and the voltage follow Ohm's law:

$$I = \frac{U_1}{R_1} + \frac{U_2}{R_2} \quad (11.1)$$

The current density (j, mA cm^{-2}) of the lateral Li flux can be calculated by normalizing it with the area of its cross-section ($w\theta_{LLZO,eff}$):

$$j = \frac{I}{w\theta_{LLZO,eff}} = \sigma_{LLZO}\left(\frac{U_1}{x_1} + \frac{U_2}{x_2}\right) \quad (11.2)$$

The effective conduction thickness in LLZO $\theta_{LLZO,eff}$ can therefore be calculated by combining eqn (8)–(11):

$$\theta_{LLZO,eff} = \frac{J_{Li\ in\ LLZO}}{w} \times \frac{F}{\sigma_{LLZO}} \times \frac{1}{\frac{U_1}{x_1} + \frac{U_2}{x_2}} \quad (12)$$

Notably, the effective conduction thickness in this calculation assumes a homogeneous current density distribution.

Simulation of lateral Li flux at the Li_3Sb/LLZO interface by the finite element method

The voltage distribution at the Li_3Sb/LLZO interface at 75 °C was simulated using the following material and electrochemical parameters: relative permittivity of LLZO of ε = 72.87 × 8.854 × 10^{-12} F m^{-1},[46] ionic conductivity of LLZO of σ_{LLZO} = 0.00216 S cm^{-1} (based on the Arrhenius equation from Fig. S2c), and potential difference between the Li metal and Sb ($E^0_{Sb/Li_2Sb} = 0.90$ V *vs.* Li^+/Li) or Li_2Sb ($E^0_{Li_2Sb/Li_3Sb} = 0.85$ V *vs.* Li^+/Li).[34] The simulation was conducted using the FEniCS computing platform[47,48] with Python 3.11. A square mesh with a size of 8 × 8 μm and a mesh resolution of 800 was created for the finite element simulation with the following boundary conditions: bottom boundary condition with a potential of 0 V and top boundary condition with a potential to create a constant vertical current density of 50 mA cm^{-2}.

The applied current density is selected to represent a regime where current focusing is pronounced and interfacial instability becomes significant, as evidenced by the critical current density measurements (Fig. 4). Under such conditions, the lateral Li flux mechanism is strongly activated and can be clearly resolved. At lower applied current densities, the same mechanism is expected to persist, but with reduced magnitude and more spatially extended flux distributions. As a result, the lateral flux features become less localized and more difficult to resolve within a finite simulation domain. Importantly, varying the applied current density primarily affects the magnitude of the flux, while preserving the qualitative behavior and spatial characteristics of lateral Li transport.

It is worth noting that the lateral Li flux depends not only on the conductivity of the SSE but also on the ion transfer across the IL/SSE interface ($R_{IL/SSE}$) and the Li conductivity within the IL itself (R_{IL}). In this study, the interfacial resistance of the Li_3Sb/LLZO interface was measured to be negligible, *ca.* 0.13 Ω cm^2 at 75 °C (Fig. 4B). Consequently, the contributions of $R_{IL/SSE}$ and R_{IL} to the lateral Li flux were determined to be minimal and were ignored in the simulation of lateral Li flux.

A Gaussian charge distribution (a point charge as the source term) ρ was created using the following equation:

$$\rho(x,y) = \frac{q}{2\pi\sigma^2}\exp\left(-\frac{(x-x_0)^2+(y-y_0)^2}{2\sigma^2}\right) \quad (13)$$

where σ is the Gaussian width, (x_0, y_0) is the position of the point charge, and q is the total charge over the mesh. To create the potential difference of a physical Li-depleted region sphere with a radius of 10 nm, the charge was set to a certain value when the voltage at a distance (r_{Sb}) of 10 nm from (x_0, y_0) was U_1 or U_2 for Li_2Sb and Li_3Sb, respectively. The position of the point charge (x_0, y_0) was set to (0, 25 nm) in the middle of the mesh and 25 nm above the bottom boundary. The Gaussian width of the simulation was set to below 0.0005, in order to get a decent resolution of the point charge. FEniCS obtains potential distribution (u) within the mesh by solving Poisson's equation:

$$\nabla^2 u = -\frac{\rho}{\varepsilon} \quad (14)$$

The Li flux distribution J can be calculated by electric field distribution E from potential u:

$$E = -\mathrm{grad}(u) \quad (15)$$

$$J = \sigma_{LLZO}\, E \quad (16)$$

Open Access Article. Published on 27 May 2026. Downloaded on 6/17/2026 4:49:48 PM.
This article is licensed under a Creative Commons Attribution-NonCommercial 3.0 Unported Licence.

The lateral current of Li flux into the Li-depleted region can be calculated by integrating current density distribution J over the lateral surface of column s surrounding the Li-depleted region:

$$I = \iint_s J \cdot \mathrm{d}s \tag{17a}$$

$$I = \int_0^y J_y \mathrm{d}y \cdot 2\pi r = \sum_0^y J_y \cdot 2\pi r \tag{17b}$$

$$\frac{\partial J_y}{\partial y} = J_y \cdot 2\pi r \tag{18}$$

where r is the radius (1.5 μm) and y is the height (8 μm) of the column as shown in Fig. 3C. Considering the amount of Sb n_{Sb} in the Li-depleted region:

$$n_{\mathrm{Sb}} = \frac{V_{\mathrm{Sb}}\rho_{\mathrm{Sb}}}{M_{\mathrm{Sb}}} = \frac{4}{3}\pi {r_{\mathrm{Sb}}}^3 \frac{\rho_{\mathrm{Sb}}}{M_{\mathrm{Sb}}} \tag{19}$$

where r_{Sb} is the radius of the depleted region (10 nm). Li consumption through the two reaction steps can be described by

$$n_{\mathrm{Sb} \rightarrow \mathrm{Li_2Sb}} = 2n_{\mathrm{Sb}} \tag{20}$$

$$n_{\mathrm{Li_2Sb} \rightarrow \mathrm{Li_3Sb}} = n_{\mathrm{Sb}} \tag{21}$$

The time to reduce the Li-depleted region t_{r} to Li_3Sb by lateral current can be estimated using the current and Li consumption:

$$t_{\mathrm{Sb}\rightarrow\mathrm{Li_2Sb}} = \frac{n_{\mathrm{Sb}\rightarrow\mathrm{Li_2Sb}}}{J_{\mathrm{Li\ in\ LLZO}}} = \frac{n_{\mathrm{Sb}\rightarrow\mathrm{Li_2Sb}}}{I_{\mathrm{Sb}}}F \tag{22}$$

$$t_{\mathrm{Li_2Sb}\rightarrow\mathrm{Li_3Sb}} = \frac{n_{\mathrm{Li_2Sb}\rightarrow\mathrm{Li_3Sb}}}{J_{\mathrm{Li\ in\ LLZO}}} = \frac{n_{\mathrm{Li_2Sb}\rightarrow\mathrm{Li_3Sb}}}{I_{\mathrm{Li_2Sb}}}F \tag{23}$$

Grazing incidence synchrotron X-ray diffraction

Grazing incidence synchrotron X-ray diffraction (GISXRD) in Fig. S9c was used to identify the structure of two distinct colored regions formed on the Sb-sputtered surface of LLZO after isostatic pressing with a Li foil. The sample was prepared by magnetron sputtering a 100 nm Sb layer onto the LLZO membrane, followed by isostatic pressing of part of the Sb-coated region with a Li foil. The sample was then heat-treated at 275 °C and immediately quenched to room temperature. Prior to GISXRD measurements, the sample was sealed in Kapton tape. GISXRD measurements were conducted at the Swiss-Norwegian Beamline (SNBL), BM01, at the European Synchrotron Radiation Facility (ESRF, Grenoble, France) using a PILATUS@SNBL diffractometer (λ = 1.03614 Å) in the high-intensity beam mode ($\sim$200 mA). The data acquisition time was 0.1 seconds per pattern, and GISXRD measurements were performed while rotating the LLZO membrane. The grazing incidence angle was determined individually for each mapping point. The measurements confirmed that the two differently colored regions formed upon isostatic pressing and heating of the Sb-sputtered LLZO surface with Li foil correspond to the formation of Li_3Sb (cubic lattice; ICSD: 44900) and Li_2Sb (hexagonal lattice; ICSD: 100020) alloys. In order to acquire enough XRD signal, the thickness of the Sb coating on LLZO for GISXRD measurements was 100 nm, which is thicker than the Sb coating for electrochemical performance and shows a different color due to the thickness effect.

Powder X-ray diffraction

XRD measurements in Fig. S2a were performed at the Swiss Norwegian Beamline (SNBL) BM01 at the European Synchrotron Radiation Facility (ESRF, Grenoble, France) using a PILATUS@SNBL diffractometer (λ = 0.68922 Å) in a high-intensity beam-mode (200 mA). The XRD pattern shows the pure cubic LLZO phase of the LLZO membranes.

Raman spectroscopy

Raman spectroscopy measurements in Fig. S3 were performed using a confocal Raman microscope (Horiba, LabRAM HR Evolution) equipped with a 532 nm Nd:Yag laser (Cobolt Samba™). To prevent exposure to air, the measured LLZO samples were sandwiched between two thin glass slides and sealed with epoxy glue inside an Ar-filled glovebox. The Raman spectra show no surface impurities on LLZO membranes.

Scanning electron microscopy and energy-dispersive X-ray spectroscopy

Scanning electron microscopy measurements of the dense LLZO membranes were performed with a Zeiss Gemini 460 using a secondary electron detector at an acceleration voltage of 5 kV and a current of 100 pA. Energy-dispersive X-ray spectroscopy of the Li/Li_3Sb/LLZO was performed with an EDS Ultim Extreme detector of the Zeiss Gemini 460 at an acceleration voltage of 10 kV and a current of 100 pA. To mitigate beam damage, the acquisition time for each spectrum was limited to 10 s.

Focused ion beam scanning electron microscopy

Focused ion beam scanning electron microscopy (FIB-SEM) cross-sectional images were obtained using a Thermo Fisher Scientific Helios 5 Laser Hydra system. Samples were loaded into the chamber with minimal air exposure. To avoid any shadow effect, a 600 μm wide cross-section was opened using a femtosecond laser at a wavelength of 1030 nm, a pulse rate of 60 kHz, and a power of 4 mJ. The resulting surface was polished using an argon plasma at 30 kV and a current of up to 0.93 μA. The images were recorded using an Everhart–Thornley detector at an acceleration voltage of 2 kV and a current of 1.6 nA with tilt correction enabled.

Electrochemical impedance spectroscopy

The Li-ion conductivity of dense LLZO membranes was measured in the temperature range of −30 °C to 100 °C. Electrochemical impedance spectroscopy (EIS) measurements were conducted using an Au/LLZO/Au symmetrical cell configuration in an ITS-e Temperature Chamber (Biologic), equipped with a CESH-e sample holder (Biologic). Au electrodes, *ca.* 50 nm

This journal is © The Royal Society of Chemistry 2026

Open Access Article. Published on 27 May 2026. Downloaded on 6/17/2026 4:49:48 PM. This article is licensed under a Creative Commons Attribution-NonCommercial 3.0 Unported Licence.

thick, were thermally evaporated onto ultrafast-sintered LLZO membranes using a Covap thermal evaporator (Angstrom). Before Au evaporation, the LLZO membranes were subjected to a post-HT at 900 °C for 10 minutes in an argon-filled glovebox using a muffle furnace. This step was performed to eliminate Li_2O contamination from the surface, as confirmed by XPS analysis. EIS measurements were carried out over a frequency range of 35 MHz to 10 Hz with an amplitude of 10 mV, using an MTZ-35 impedance analyzer (Biologic). The ionic conductivities (σ, S cm^{-1}) were calculated based on the total resistance (R, Ω) values of the dense LLZO membranes, considering their thickness (l = 45 μm) and the surface area of the Li electrodes (S = 0.12566 cm^2), using the following equation:

$$\sigma = \frac{l}{R \times S} \tag{24}$$

The activation energy in Fig. S2c was calculated using the Arrhenius equation:

$$\sigma T = A e^{-E_a/k_B T} \tag{25}$$

where A is the pre-exponential factor, E_a (eV) is the activation energy for ionic conduction, T (K) is the temperature, and k_B (eV K^{-1}) is the Boltzmann constant.

Preparation of Li/LLZO/Li and Li/Li_3Sb/LLZO/Li_3Sb/Li symmetrical cells

Symmetrical cells were prepared by cold isostatic pressing of Li foil discs (71 MPa for 3 minutes) on both sides of as-prepared or Sb (10 nm)-coated LLZO membranes in an inert environment using a PW 100 EH cold isostatic press (P/P/Weber). The Li foil was prepared by cutting a Li metal rod into small pieces, rolling them on a stainless-steel substrate to a thickness of *ca.* 100 μm, and then cutting 4 mm discs from the resulting foil. The Li/Li_3Sb/LLZO/Li_3Sb/Li cells were then heated at 275 °C for 30 min on a heating plate in an Ar-filled glovebox to form the Li_3Sb IL.

Electrochemical measurements of the symmetrical cells were conducted at 75 °C in a sealed vacuum furnace integrated into an argon-filled glovebox and connected to a BioLogic VMP-300 multichannel workstation. EIS measurements were performed in the frequency range of 10 Hz to 7 MHz with an amplitude of 10 mV using the BioLogic VMP-300 multichannel workstation.

The steps of critical current density measurements are as follows: a step of 0.1 mA cm^{-2} from 0.1 to 2.0 mA cm^{-2}, a step of 0.2 mA cm^{-2} from 2.0 to 5.0 mA cm^{-2}, a step of 0.5 mA cm^{-2} from 5.0 to 15.0 mA cm^{-2}, a step of 1.0 mA cm^{-2} from 15 to 20 mA cm^{-2}, and a step of 10 mA cm^{-2} from 20 to 100 mA cm^{-2}.

Preparation of the NMC811-LPSCl cathode

A 5 wt% stock solution of hydrogenated nitrile butadiene rubber (HNBR, Therban® LT 1707, Arlanexeo) binder was prepared by dissolving HNBR (8.76 g) in 200 mL of toluene and stirring the solution for 24 h. In parallel, the purchased powders of $LiNbO_3$ (LNO)@NMC811 (KRI Inc.), Li_6PS_5Cl (LPSCl, D_{50} = 3 μm, Wellcos), and vapor-grown carbon fiber (VGCF, 99.99%, fiber diameter 150 nm, fiber length 4 μm, Resonac) were transferred to a glass jar and stirred with a spatula until a homogeneous powder mixture was obtained. Then, the powder mixture was mixed with toluene solution of HNBR binder, toluene and IBIB solvents using an ULTRA TURRAX homogenizer (IKA, ULTRA TURRAX T18) at 6000 rpm for 3 min and then at 10 000 rpm for 3 min. The target mass ratio of LNO@NMC811 : LPSCl : VGCF : HNBR was 67.5 : 29.0 : 3.0 : 0.5. The volume ratio of toluene (>99.5%, Roth):isobutyl isobutyrate (IBIB, >98%, Sigma Aldrich) was 1 : 1. The resulting slurry was tape cast onto a carbon-coated Al foil in an Ar-filled glovebox using a 200 μm opening doctor blade, followed by drying overnight at room temperature. The NMC811 loading was 12 mg cm^{-2}.

Fabrication of the NMC811-LPSCl/LLZO/Li_3Sb/Li full cell

The fabrication of NMC811-LPSCl/LLZO/Li_3Sb/Li all-solid-state batteries involved several steps. First, one side of the as-fabricated LLZO membrane was sputter-coated with a 10 nm Sb film, followed by isostatic pressing with a Li foil at 71 MPa for 3 minutes. The assembly was then heat-treated at 275 °C for 30 minutes to form the Li_3Sb interlayer. Next, 4 mm diameter cathode disks were punched from the NMC811-LPSCl cathode and isostatically pressed onto the opposite side of the LLZO membrane at 160 MPa for 3 minutes. Electrochemical measurements of the assembled full cells were performed at 75 °C under a pressure of 1 MPa using a home-made cell-setup in an Ar-filled glovebox, within a voltage range of 3.0–4.3 V *vs.* Li^+/Li, using a BioLogic VMP-300 multichannel workstation.

Energy density calculations

The schematic of the all-solid-state battery used for gravimetric and volumetric energy density calculations is shown in Fig. S22. The calculations assumed 100% utilization of the NMC811 active material, an average cell voltage of 3.8 V, and the total weight or volume of all cell components. The all-solid-state cathode composition was considered as 70 wt% NMC811, 28 wt% Li_6PS_5Cl (LPSCl), and 2 wt% carbon additives. The battery configuration included a 10 μm Li metal anode, a 12 μm Cu foil anode current collector, and a 16 μm Al foil cathode current collector. The thickness of the LLZO solid-state separator and the areal capacity of the all-solid-state cathode electrolyte were varied, ranging from 8 to 500 μm and 1 to 5 mAh cm^{-2}, respectively. All parameters used for the energy density calculations are summarized in Table S2.

Author contributions

HZ and FO contributed equally. Conceptualization: HZ, KVK, and MVK. Methodology: HZ, FO, KVK, and MVK. Investigation: HZ, FO, MK, JFB, JS, AM, IN, and OK. Funding acquisition: OV, YER, KVK, and MVK. Supervision: KVK, OV, YER, and MVK.

Open Access Article. Published on 27 May 2026. Downloaded on 6/17/2026 4:49:48 PM. This article is licensed under a Creative Commons Attribution-NonCommercial 3.0 Unported Licence.

Writing – original draft: HZ and KVK. Writing – review & editing: HZ, FO, JB, OV, KVK, and MVK.

Conflicts of interest

There are no conflicts to declare.

Data availability

All data supporting the findings of this study are available within the paper and supplementary information (SI). Source data are provided with this paper. Supplementary information: Notes S1–S3, Fig. S1–S22, Tables S1 and S2, and Videos S1–S4. See DOI: https://doi.org/10.1039/d6ee02327d.

Acknowledgements

The authors are grateful for access to the Swiss Norwegian beamlines at the ESRF and thank their staff: Charles J. McMonagle, Vadim Dyadkin, Dmitry Chernyshov, and Wouter van Beek, for excellent support during the experiments. The authors are grateful for access to the research facilities at ETH Zurich, specifically the Scientific Center for Optical and Electron Microscopy and the Small Molecule Crystallography Center. They also acknowledge the research resources at Empa, particularly the Electron Microscopy Center. The authors thank Suwen Jin for technical support with Python coding. This work is financially supported by the Swiss Innovation Agency (Innosuisse) under grant agreement (Grant 58207.1) and the Swiss National Science Foundation (grant no. 200021-232329). IN, OK, OV acknowledge the support from Natural Sciences and Engineering Research Council of Canada (Discovery grant 2024-05613) and Digital Research Alliance of Canada.

References

1 M. D. Gao, H. Li, L. Xu, Q. Xue, X. N. Wang, Y. Bai and C. Wu, *J. Energy Chem.*, 2021, **59**, 666–687.
2 A. Banerjee, X. F. Wang, C. C. Fang, E. A. Wu and Y. S. Meng, *Chem. Rev.*, 2020, **120**, 6878–6933.
3 F. D. Han, A. S. Westover, J. Yue, X. L. Fan, F. Wang, M. F. Chi, D. N. Leonard, N. Dudney, H. Wang and C. S. Wang, *Nat. Energy*, 2019, **4**, 187–196.
4 F. Shen, M. B. Dixit, X. Xiao and K. B. Hatzell, *ACS Energy Lett.*, 2018, **3**, 1056–1061.
5 D. W. Wang, K. Y. Peng, Y. P. Fu, C. B. Zhu and Y. Yang, *J. Power Sources*, 2021, **487**, 229421.
6 R. H. Brugge, A. K. O. Hekselman, A. Cavallaro, F. M. Pesci, R. J. Chater, J. A. Kilner and A. Aguadero, *Chem. Mater.*, 2018, **30**, 3704–3713.
7 K. Hofstetter, A. J. Samson, S. Narayanan and V. Thangadurai, *J. Power Sources*, 2018, **390**, 297–312.
8 Y. Wang and W. Lai, *J. Power Sources*, 2015, **275**, 612–620.
9 T. Krauskopf, B. Mogwitz, C. Rosenbach, W. C. Zeier and J. Janek, *Adv. Energy Mater.*, 2019, **9**, 1902568.
10 Z. X. Wang, Y. Lu, C. Z. Zhao, W. Z. Huang, X. Y. Huang, W. J. Kong, L. X. Li, Z. Y. Wang, H. Yuan, J. Q. Huang and Q. Zhang, *Joule*, 2024, **8**, 2794–2810.
11 X. M. Liu, R. Garcia-Mendez, A. R. Lupini, Y. Q. Cheng, Z. D. Hood, F. D. Han, A. Sharafi, J. C. Idrobo, N. J. Dudney, C. S. Wang, C. Ma, J. Sakamoto and M. F. Chi, *Nat. Mater.*, 2021, **20**, 1485.
12 J. S. Kim, H. Kim, M. Badding, Z. Song, K. Kim, Y. Kim, D. J. Yun, D. Lee, J. Chang, S. Kim, D. Im, S. Park, S. H. Kim and S. Heo, *J. Mater. Chem. A*, 2020, **8**, 16892–16901.
13 V. Raj, K. G. Naik, B. S. Vishnugopi, A. K. Rana, A. S. Manning, S. R. Mahapatra, K. Varun, V. Singh, A. Nigam, J. D. Mcbrayer, P. P. Mukherjee, N. P. B. Aetukuri and D. Mitlin, *Adv. Energy Mater.*, 2024, **14**, 2303062.
14 Q. S. Tu, L. Barroso-Luque, T. Shi and G. Ceder, *Cell. Rep. Phys. Sci.*, 2020, **1**, 100106.
15 M. Klimpel, H. Y. Zhang, G. Paggiaro, R. Dubey, F. Okur, L. P. H. Jeurgens, K. V. Kravchyk and M. V. Kovalenko, *Adv. Mater. Interfaces*, 2024, **11**, 2300948.
16 H. P. Zheng, S. P. Wu, R. Tian, Z. M. Xu, H. Zhu, H. N. Duan and H. Z. Liu, *Adv. Funct. Mater.*, 2020, **30**, 1906189.
17 H. Y. Zhang, G. Paggiaro, F. Okur, J. Huwiler, C. Cancellieri, L. P. H. Jeurgens, D. Chernyshov, W. van Beek, M. V. Kovalenko and K. V. Kravchyk, *ACS Appl. Energy Mater.*, 2023, **6**, 6972–6980.
18 A. Sharafi, E. Kazyak, A. L. Davis, S. H. Yu, T. Thompson, D. J. Siegel, N. P. Dasgupta and J. Sakamoto, *Chem. Mater.*, 2017, **29**, 7961–7968.
19 B. B. Wu, S. Y. Wang, J. Lochala, D. Desrochers, B. Liu, W. Q. Zhang, J. H. Yang and J. Xiao, *Energy Environ. Sci.*, 2018, **11**, 1803–1810.
20 L. C. Wang, J. X. Wu, C. S. Bao, Z. C. You, Y. Lu and Z. Y. Wen, *Susmat*, 2024, **4**, 72–105.
21 K. V. Kravchyk, D. T. Karabay and M. Kovalenko, *Sci. Rep.*, 2022, **12**, 1177.
22 X. Xiang, Y. H. Zhang, H. H. Wang, C. H. N. Wei, F. Chen and Q. Shen, *J. Electrochem. Soc.*, 2021, **168**, 060515.
23 Y. L. Luo, W. W. Feng, Z. J. Meng, Y. J. Wang, X. Jiang and Z. H. Xue, *Electrochim. Acta*, 2021, **397**, 139285.
24 C. L. Tsai, V. Roddatis, C. V. Chandran, Q. L. Ma, S. Uhlenbruck, M. Bram, P. Heitjans and O. Guillon, *ACS Appl. Mater. Interfaces*, 2016, **8**, 10617–10626.
25 J. S. Kim, G. Yoon, S. Kim, S. Sugata, N. Yashiro, S. Suzuki, M. J. Lee, R. Kim, M. Badding, Z. Song, J. M. Chang and D. Im, *Nat. Commun.*, 2023, **14**, 782.
26 T. Panneerselvam, R. Murugan and O. V. Sreejith, *ACS Appl. Energy Mater.*, 2024, **7**, 1700–1709.
27 R. Dubey, J. Sastre, C. Cancellieri, F. Okur, A. Förster, L. Pompizii, A. Priebe, Y. E. Romanyuk, L. P. H. Jeurgens, M. V. Kovalenko and K. V. Kravchyk, *Adv. Energy Mater.*, 2021, **11**, 2102086.
28 W. Luo, Y. H. Gong, Y. Z. Zhu, K. K. Fu, J. Q. Dai, S. D. Lacey, C. W. Wang, B. Y. Liu, X. G. Han, Y. F. Mo, E. D. Wachsman and L. B. Hu, *J. Am. Chem. Soc.*, 2016, **138**, 12258–12262.
29 G. Q. Zhao, C. W. Luo and Q. S. Hua, *J. Mater. Chem. A*, 2023, **11**, 20174–20186.

 This journal is © The Royal Society of Chemistry 2026

Open Access Article. Published on 27 May 2026. Downloaded on 6/17/2026 4:49:48 PM.
This article is licensed under a Creative Commons Attribution-NonCommercial 3.0 Unported Licence.

30 V. Raj, V. Venturi, V. R. Kankanallu, B. Kuiri, V. Viswanathan and N. P. B. Aetukuri, *Nat. Mater.*, 2022, **21**, 1050.
31 S. M. Zhang, B. K. Hu, Z. Y. Geng, X. W. Gao, D. Spencer-Jolly, D. L. R. Melvin, Z. Y. Ning, G. C. Li, M. Jenkins, L. L. Wang, H. Gao, S. D. Pu, T. J. Marrow, C. W. Monroe and P. G. Bruce, *Energy Environ. Sci.*, 2024, **17**, 1448–1456.
32 M. Yahyaoglu, T. Soldi, M. Ozen, C. Candolfi, G. J. Snyder and U. Aydemir, *J. Mater. Chem. A*, 2021, **9**, 25024–25031.
33 W. Weppner and R. A. Huggins, *J. Electrochem. Soc.*, 1977, **124**, 1569.
34 M. He, K. Kraychyk, M. Walter and M. V. Kovalenko, *Nano Lett.*, 2014, **14**, 1255–1262.
35 J. G. Connell, T. Fuchs, H. Hartmann, T. Krauskopf, Y. S. Zhu, J. Sann, R. Garcia-Mendez, J. Sakamoto, S. Tepavcevic and J. Janek, *Chem. Mater.*, 2020, **32**, 10207–10215.
36 J. H. Li and R. G. Wang, *Ceram. Int.*, 2021, **47**, 13280–13290.
37 F. Okur, H. Y. Zhang, J. F. Baumgärtner, J. Sivavec, M. Klimpel, G. P. Wasser, R. Dubey, L. P. H. Jeurgens, D. Chernyshov, W. van Beek, K. V. Kravchyk and M. V. Kovalenko, *Adv. Sci.*, 2025, **12**, 2412370.
38 W. L. Feng, X. L. Dong, P. L. Li, Y. G. Wang and Y. Y. Xia, *J. Power Sources*, 2019, **419**, 91–98.
39 K. Fu, Y. H. Gong, Z. Z. Fu, H. Xie, Y. G. Yao, B. Y. Liu, M. Carter, E. Wachsman and L. B. Hu, *Angew. Chem., Int. Ed.*, 2017, **56**, 14942–14947.
40 G. Kresse and J. Furthmuller, *Comp. Mater. Sci.*, 1996, **6**, 15–50.
41 J. P. Perdew, K. Burke and M. Ernzerhof, *Phys. Rev. Lett.*, 1996, **77**, 3865–3868.
42 J. P. Perdew, M. Ernzerhof and K. Burke, *J. Chem. Phys.*, 1996, **105**, 9982–9985.
43 G. Kresse and D. Joubert, *Phys. Rev. B:Condens. Matter Mater. Phys.*, 1999, **59**, 1758–1775.
44 Z. Deng, Z. Y. Zhu, I. H. Chu and S. P. Ong, *Chem. Mater.*, 2017, **29**, 281–288.
45 S. P. Ong, W. D. Richards, A. Jain, G. Hautier, M. Kocher, S. Cholia, D. Gunter, V. L. Chevrier, K. A. Persson and G. Ceder, *Comput. Mater. Sci.*, 2013, **68**, 314–319.
46 R. F. Samsinger, M. Letz, J. Schuhmacher, M. Schneider, A. Roters, D. Kienemund, H. Maune and A. Kwade, *J. Electrochem. Soc.*, 2020, **167**, 140510.
47 M. Alnæs, J. Blechta, J. Hake, A. Johansson, B. Kehlet, A. Logg, C. Richardson, J. Ring, M. E. Rognes and G. N. Wells, *Arch. Numer. Softw.*, 2015, **3**, 9–23.
48 A. Logg, K.-A. Mardal and G. N. Wells, *Automated Solution of Differential Equations by the Finite Element Method*, Springer, 2012.